

# UC Berkeley

## UC Berkeley Previously Published Works

### Title

Preferred orientation in experimentally deformed stishovite: implications for deformation mechanisms

### Permalink

<https://escholarship.org/uc/item/54r3w6c5>

### Journal

Physics and Chemistry of Minerals, 42(4)

### ISSN

0342-1791

### Authors

Kaercher, Pamela M  
Zepeda-Alarcon, Eloisa  
Prakapenka, Vitali B  
[et al.](#)

### Publication Date

2015-04-01

### DOI

10.1007/s00269-014-0718-5

Peer reviewed

# Preferred orientation in experimentally deformed stishovite: implications for deformation mechanisms

Pamela M. Kaercher · Eloisa Zepeda-Alarcon · Vitali B. Prakapenka · Waruntorn Kanitpanyacharoen · Jesse S. Smith · Stanislav Sinogeikin · Hans-Rudolf Wenk

Received: 26 June 2014 / Accepted: 21 October 2014 / Published online: 7 November 2014  
© Springer-Verlag Berlin Heidelberg 2014

**Abstract** Although the crystal structure of the high-pressure SiO<sub>2</sub> polymorph stishovite has been studied in detail, little is known about the development of crystallographic preferred orientation (CPO) during deformation in stishovite. Insight into CPO and associated deformation mechanics of stishovite would provide important information for understanding subduction of quartz-bearing crustal rocks into the mantle. To study CPO development, we converted a natural sample of flint to stishovite in a laser-heated diamond anvil cell and compressed the stishovite aggregate up to 38 GPa. We collected diffraction patterns in radial geometry to examine in situ development of crystallographic preferred orientation and find that (001) poles preferentially align with the compression direction. Viscoplastic self-consistent modeling suggests the most likely slip systems at high pressure and ambient temperature are pyramidal and basal slip.

**Keywords** Stishovite · Preferred orientation · Diamond anvil cell · Slip systems · High pressure/stress

## Introduction

Stishovite is a polymorph of SiO<sub>2</sub> present in the mantle, making its deformation properties relevant to Earth science. Stishovite was first produced experimentally (Stishov and Popova 1961) and found to have a rutile structure (space group P4<sub>2</sub>/mnm, Stishov and Belov 1962; Sinclair and Ringwood 1978; Ross et al. 1990) with its silicon in octahedral rather than tetrahedral coordination, as is characteristic of lower-pressure SiO<sub>2</sub> polymorphs. Stishovite has since been documented in meteorites such as the Shergotty (El Goresy et al. 2004); at meteorite impact sites such as Ries Crater, Germany (Shoemaker and Chao 1961; Chao and Littler 1963), Meteor Crater, Arizona, USA (Chao et al. 1962), and Vredefort crater, South Africa (Martini 1978, 1991); and in high-pressure metamorphic environments (Liu et al. 2007). First principles calculations (e.g., Cohen 1991; Karki et al. 1997; Teter et al. 1998; Lee and Gonze 1997), Landau theory (Carpenter et al. 2000), Raman spectroscopy experiments (e.g., Kingma et al. 1995), and X-ray diffraction experiments (e.g., Tsuchida and Yagi 1989; Ross et al. 1990; Kingma et al. 1996; Andrault et al. 1998; Hemley et al. 2000) find stishovite to be stable from ~10 to 50 GPa, corresponding to 300–1,200 km depth in the Earth, so a significant portion of the upper and lower mantle. Stishovite is inferred to exist in the upper mantle from inclusions in diamond (Joswig et al. 1999) where quartz is likely transported in subducting slabs as a component in sedimentary layers and mid-ocean ridge basalts and converted to stishovite (Irifune and Ringwood 1993). Acoustic velocity measurements through a single crystal find stishovite to be elastically anisotropic (Yoneda et al. 2012). Thus, if stishovite develops crystallographic preferred orientation (CPO), it may contribute to seismic anomalies in the mantle (Vinnik et al. 2001; Asahara et al. 2013), yet little is known

---

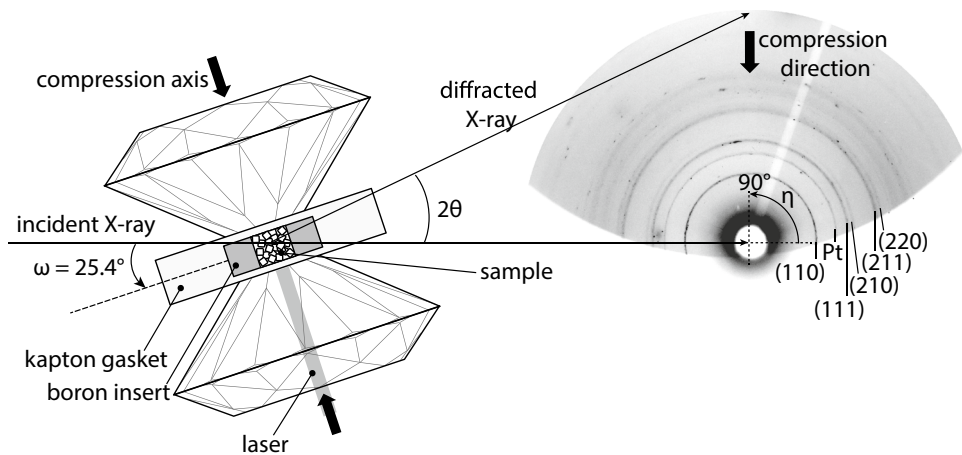
P. M. Kaercher (✉) · E. Zepeda-Alarcon · H.-R. Wenk  
Department of Earth and Planetary Science, University of California, Berkeley, Berkeley, CA, USA  
e-mail: p.kaercher@berkeley.edu

V. B. Prakapenka  
Center for Advanced Radiation Sources, University of Chicago, Chicago, IL, USA

W. Kanitpanyacharoen  
Department of Geology, Faculty of Science, Chulalongkorn University, Bangkok, Thailand

J. S. Smith · S. Sinogeikin  
HPCAT, Geophysical Laboratory, Carnegie Institution of Washington, Argonne, IL, USA

**Fig. 1** Experimental setup for diamond anvil cell (DAC) in radial geometry for Run 2. The DAC was tilted  $25.4^\circ$  to reduce interference from the gasket; however, the cell also obscures the bottom of the diffraction pattern when tilted at this angle. The raw diffraction pattern shown on the right is of stishovite at 38 GPa (#182, Table 1)



about the active deformation mechanisms of stishovite at high pressure, which provide important information for understanding subduction of quartz-bearing crustal rocks into the mantle.

Previous studies of plastic deformation mechanisms in stishovite by transmission electron microscopy (e.g., Cordier et al. 2004; Texier and Cordier 2006) and in isostructural minerals rutile,  $\text{TiO}_2$  (Ashbee and Smallman 1963), and paratellurite,  $\text{TeO}_2$  (Péter et al. 1986), are contradictory. Examination of dislocations and theoretical calculations leads Cordier et al. (2004) and Texier and Cordier (2006) to predict prismatic slip as the dominant mechanism in stishovite, Ashbee and Smallman (1963) to suggest pyramidal slip in rutile and Péter et al. (1986) to propose basal slip in paratellurite. To better understand plastic deformation by slip in stishovite aggregates, we transformed quartz to stishovite and then deformed it at ambient temperature at pressures up to 38 GPa in a diamond anvil cell (DAC) in radial diffraction geometry while documenting the evolution of CPO. We infer deformation mechanisms leading to the observed CPO by comparing experimental CPO patterns with viscoplastic self-consistent (VPSC) polycrystal plasticity models (Lebensohn and Tomé 1994).

## Experiments

Experiments were performed on flint from nodules in Cretaceous limestones gathered along the coast of Norfolk, UK. The flint was ground for roughly 10 h in order to achieve a crystallite size small enough to reliably analyze diffraction patterns. Coherently scattering domains within grains (i.e., crystallite sizes) were measured to be  $\sim 40$  nm and provide a lower bound for grain size; crystallite sizes were determined from peak shapes in X-ray diffraction patterns after calibrating with either a  $\text{CeO}_2$  or  $\text{LaB}_6$  standard to account for instrument broadening. Stishovite was

synthesized from the flint and compressed in two experimental DAC runs up to 23 and 38 GPa at HPCAT (sector 16-ID-B) and GSECARS (sector 13-ID-D) beamlines, respectively, of the Advanced Photon Source (APS) at Argonne National Laboratory. We laser-heated samples at pressures of 13–16 GPa in order to activate kinetics and transition quartz directly to stishovite without first transitioning to coesite or intermediate metastable  $\text{SiO}_2$  phases that have previously been observed to nucleate at room temperature and  $\sim 21$  GPa (e.g., Haines et al. 2001; Kingma et al. 1996; Prakapenka et al. 2004). We performed experiments in radial diffraction geometry (e.g., Wenk et al. 2006) rather than axial geometry in order to see variations in diffraction intensities as a function of the azimuthal angle  $\eta$  on Debye rings (the angle with respect to the compression direction;  $\eta = 90^\circ$  is labeled in Fig. 1).

## Run 1

The first run was performed at HPCAT beamline 16-ID-B in a modified Mao-Bell DAC with  $70^\circ$  lateral openings for radial diffraction (Liermann et al. 2009). The sample was loaded into a boron epoxy gasket inside of a Kapton insert (Merkel and Yagi 2005). A larger sample chamber,  $\sim 80$   $\mu\text{m}$  in diameter and initially  $\sim 50$   $\mu\text{m}$  in depth, was used since quartz does not diffract strongly and pressures needed to synthesize stishovite are relatively low ( $\sim 10$  GPa) for the DAC. The diamond culets were 300  $\mu\text{m}$  in diameter. No pressure medium was used in order to impose deviatoric stress on the sample and promote development of CPO. Pressure was increased with a helium gas membrane system that drives the piston of the DAC. A  $\sim 15$ - $\mu\text{m}$  diameter,  $\sim 5$ - $\mu\text{m}$  thick Pt flake placed on the bottom of the sample chamber was used both as a pressure marker and to enhance absorption of the laser spot to heat the sample. The sample was placed  $\sim 300$  mm from the detector, and a monochromatic beam with wavelength 0.4066 Å and spot size of 4  $\mu\text{m} \times 5$   $\mu\text{m}$  was aligned with the sample. Diffraction

patterns were collected for 40–120 s on a Mar345 imaging plate detector binned to  $3,450 \times 3,450$  with pixel size 0.1 mm. Instrument parameters such as detector centering and tilt were calibrated with a  $\text{CeO}_2$  standard.

The sample was compressed to 13 GPa, then laser heated using the portable Nd:YLF double-sided laser heating setup at 16-ID-B (Shen et al. 2010). A temperature reading could not be collected, but is estimated to be  $\sim 1,500$ – $2,000$  K. We rastered across the sample for 40 min with a  $15\text{-}\mu\text{m}$ -diameter flat top laser beam, causing quartz to partially transform to stishovite. Initial partial transformation may be due to pressure gradients across the sample, which is typical of radial diffraction DAC experiments. In addition, heating was not completely uniform throughout the sample due to placement of the laser absorbing Pt flake at one end of the sample chamber, and some temperature heterogeneities existed as well. After increasing pressure to 23 GPa at ambient temperature, quartz fully converted to stishovite.

## Run 2

A second run was done at GSECARS beamline 13-ID-D in a modified symmetric DAC with side openings  $60^\circ$  wide for radial diffraction. The cell was tilted such that the compression axis was  $64.6^\circ$  from the incoming X-rays (Fig. 1) in order to reduce noise from the boron epoxy gasket (Lin et al. 2010). The sample chamber was again  $\sim 80\ \mu\text{m}$  in diameter and  $\sim 50\ \mu\text{m}$  in depth, diamond culets were  $300\ \mu\text{m}$ , and no pressure medium was used. As in Run 1, pressure was increased with a helium gas membrane system, and a Pt flake was used as a pressure marker and to couple with the laser for heating. The sample-to-detector distance was approximately 200 mm. An X-ray beam with wavelength  $0.3344\ \text{\AA}$  and diameter of  $\sim 3\ \mu\text{m}$  was focused on the sample, and diffraction patterns were collected for 60 s on a Mar165 charge-coupled device (CCD) detector binned to  $2,048 \times 2,048$  with pixel size 0.079 mm. Instrument parameters were calibrated with  $\text{LaB}_6$ . For materials with relatively low-angle diffraction peaks such as quartz and stishovite,  $\text{LaB}_6$  is preferred over  $\text{CeO}_2$  because of diffraction peaks at lower angles.

Initial pressure in the closed DAC was 16 GPa. The flint was heated at this pressure with flat top laser beams of  $25\ \mu\text{m}$  in diameter for 5 min using the fiber laser heating system at 13-ID-D (Prakapenka et al. 2008). A Princeton spectrometer with a PIXIS detector measured the blackbody radiation from which the maximum temperature was measured to be  $\sim 2,200$  K. Following heating, sample pressure dropped to 15 GPa; stishovite was not yet seen in diffraction patterns. Pressure was then increased in  $\sim 5$  GPa steps, while diffraction patterns were taken at  $2\text{-}\mu\text{m}$  intervals across the laser-heated sample area. As in Run 1, some

heterogeneities existed due to uneven heating from placement of Pt at one end of the sample chamber. At 23 GPa, quartz partially converted to stishovite, and at the highest pressure in Run 2, 38 GPa, quartz had fully converted to stishovite.

## Data analysis

Diffraction patterns were analyzed using Rietveld refinement (Rietveld 1969), which is a least-squares method that minimizes the difference between the data and a calculated fit by refining backgrounds, phase volume fractions, cell parameters, crystallite size, root-mean-square (r.m.s.) microstrain, differential stress, and CPO. The Rietveld method was implemented in the software MAUD (Material Analysis Using Diffraction, Lutterotti et al. 1997; Wenk et al. 2014). Before analysis in MAUD, diffraction images were unrolled in Fit2D (Hammersley et al. 1996), with diffraction intensity integrated over  $5^\circ$  sectors along the azimuthal angle  $\eta$  for a total of 72 spectra per diffraction image for Run 1 and 36 spectra per diffraction image for Run 2.

For Run 2, the bottom of the tilted DAC blocked diffracted X-rays from reaching the detector, and Debye rings from  $\eta \approx 0^\circ$  to  $180^\circ$  only could be collected (Fig. 1). While  $90^\circ$  in  $\eta$  is enough to see all crystal orientations relative to compression,  $360^\circ$  is preferred for textural analysis as it provides better counting statistics and diminishes influence from artifacts, such as bright intensity spots from large grains. To maintain better counting statistics, two ( $180^\circ$ ) diffraction patterns taken at different locations in the sample were analyzed at each pressure for Run 2. Since the DAC in Run 2 was rotated  $25.4^\circ$  in  $\omega$  such that the incoming X-ray path was no longer perpendicular to the compression direction (see Fig. 1),  $\omega = 25.4^\circ$  was defined for all spectra in the dataset in MAUD.

Integrated 2D plots are shown in Fig. 2 with data in the bottom half of each plot, and the calculated fit on top. The calculated diffraction patterns derive from the experimentally determined structure for quartz (from the MAUD database, space group  $\text{P3}_121$ ) and stishovite (Ross et al. 1990, crystallographic information file # 9001276), with corrections made for the background. Backgrounds were fit with a fourth-order polynomial. Diffuse background peaks at low  $2\theta$  from the Kapton insert seen near  $2\theta = 6.8^\circ$  in Run 1 (Fig. 2) were fit with two background peaks at  $\eta = 90^\circ$  and  $\eta = 270^\circ$ . A  $2\theta$  range of  $6.8^\circ$ – $21^\circ$  was used in analysis of data from Run 1, and  $5.5^\circ$ – $17.8^\circ$ , for Run 2 because of high intensity scattering from gasket material present at lower angles and clipping of diffraction peaks by the DAC windows at higher angles. Cell parameters, crystallite size, microstrain, microstress and crystallographic orientation distribution were then refined until peak position, peak

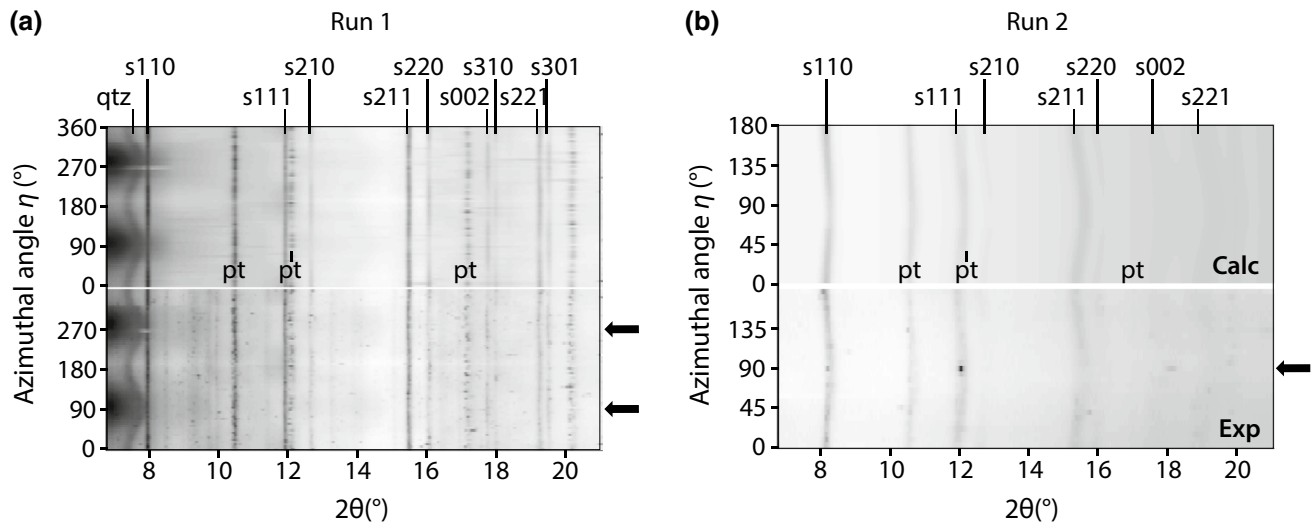


**Fig. 2** Unrolled diffraction images from **a** Run 1 at 13 GPa (#40) and **b** Run 2 at 38 GPa (#182). The *bottom half* of each pattern is the experimental data (Exp), and the top is the calculated fit (Calc). Compression direction is denoted with arrows. Regular intensity variations with azimuthal angle  $\eta$  denotes CPO. Note, for example, the stronger

intensity around  $\eta = 90^\circ$  and  $\eta = 270^\circ$  in stishovite peak 002 (s002) in (a), consistent with preferred orientation of [001] poles parallel to compression. In Run 1, the DAC was not tilted, and gasket peaks can be seen in the *bottom half* of (a)

width and variations in peak position and intensity with azimuthal angle  $\eta$  provided a close match with experiment.

The hydrostatic pressure was determined as a function of volume change with a Birch Murnaghan equation of state for quartz (Angel et al. 1997) and for stishovite (Wang et al. 2012). Volume was calculated from the cell parameters, which are determined by the hydrostatic peak position (taken at  $\eta = 54.7^\circ$  from the compression direction, described in Singh et al. 1998) along  $2\theta$  (Fig. 2). In both experiments the DACs were closed and the samples were already at pressure for the first diffraction measurements; thus, we used ambient pressure volume  $112.981 \text{ \AA}^3$  for quartz (Angel et al. 1997) and  $46.55 \text{ \AA}^3$  for stishovite (Wang et al. 2012) when determining pressures. The isotropic size strain model was used to fit the peak widths by refining the parameters crystallite size and r.m.s. micro-strain (Lutterotti and Scardi 1990).

Sinusoidal variations in peak position with azimuthal angle  $\eta$  (e.g., quartz at  $2\theta = 7.5^\circ$  in Fig. 2a) are due to elastic strain in response to differential stress. Differential stress is defined as  $t = \sigma_{33} - \sigma_{11}$  (Singh et al. 1998) where  $\sigma_{33}$  is the axial stress component, which decreases  $d$ -spacing in the compression direction, and  $\sigma_{11} = \sigma_{22}$  are the stress components perpendicular to compression (and equal due to axial symmetry), which increase  $d$ -spacing in the direction perpendicular to compression. The Moment Pole Stress model (Matthies et al. 2001; Wenk et al. 2014) was used to calculate principal stresses  $\sigma_{11}$  and  $\sigma_{33}$  from variations in peak position by using the BulkPathGeo stress/strain averaging model (Matthies et al. 2001) and elastic

constants of quartz (Kimizuka et al. 2007) and stishovite (Jiang et al. 2009) as a function of pressure.

In addition to elastic strain, non-hydrostatic (differential) stress also imposes plastic strain, which can lead to CPO, manifested as variations in peak intensity with  $\eta$  in diffraction patterns. Variations in intensity are best viewed in unrolled diffraction patterns and are especially apparent in the 220 and 002 stishovite peaks in Fig. 2a. Texture, i.e., CPO, was fit using the E-WIMV algorithm, an extension of the WIMV algorithm (Matthies and Vinel 1982). We chose an orientation distribution function (ODF) resolution of  $15^\circ$ . Textures were observed to be approximately axially symmetric about the compression direction, consistent with the compression geometry and placement of the sample in the center of the culets; thus, textures were refined again with enforced cylindrical (also known as fiber) symmetry in MAUD. The resulting ODF was processed and smoothed in the software program BEARTEX (Wenk et al. 1998) to create the inverse pole figures (IPFs) shown in Fig. 4.

## Results

A summary of crystallite size, differential stress  $t$  (which is negative for compression), and texture strength given in multiples of random distribution (m.r.d.) as a function of pressure is shown in Table 1. Standard deviations are shown in parentheses. Standard deviations are based on the least-squares fit, and actual uncertainties are small for parameters that are well constrained by diffraction data,

**Table 1** A summary of cell parameters, crystallite size, differential stress ( $t$ ), and texture sharpness given in m.r.d. as a function of pressure ( $P$ )

	Image	Phase	$a$ (Å)	$c$ (Å)	$P$ (GPa)	Crystallite size (nm)	$t$ (GPa)	Pole density (m.r.d.)	
								min.	max.
Run 1	9	q	4.762 (1)	5.408 (2)	2	47.4 (7)	−4.28 (2)	0.88	1.11
	37	q	4.476 (1)	5.158 (2)	13	41.3 (7)	−6.56 (2)	0.74	1.32
	40, 41	q*	4.499 (4)	5.128 (8)	13	47.6 (7)	−5.22 (6)	0.52	1.85
		s*	4.12386 (8)	2.6404 (1)					
48	s	4.0797 (3)	2.6189 (5)	23	20.5 (4)	−8.31 (9)	0.50	2.42	
Run 2	19, 24	q	4.4372 (6)	5.121 (1)	16	10.5 (1)	−5.37 (3)	0.80	1.23
	65, 83	q*	4.4573 (5)	5.138 (1)	15	11.3 (2)	−4.83 (3)	0.84	1.17
	113, 123	q	4.3560 (8)	5.059 (2)	21	9.1 (1)	−4.89 (3)	0.66	1.36
		s	4.0798 (2)	2.6176 (4)					
178, 182	s	4.0302 (3)	2.5888 (5)	38	24.8 (1)	−14.0 (1)	0.70	2.28	

Image numbers correspond to diffraction patterns in Fig. 3 and IPFs in Fig. 4. Phases quartz ( $q$ ) and stishovite ( $s$ ) with an asterisk denote diffraction patterns collected just after laser heating. Minimum and maximum m.r.d. for inverse pole figures (IPFs) in Fig. 4 are listed in the two right-most columns. Numbers in parentheses are standard deviations

such as lattice parameters. For less constrained parameters, such as grain size, actual errors may be much larger (Toby 2006). In radial diffraction geometry, the X-ray beam passes through the perimeter and center of the sample chamber and, if a gradient of pressures and stresses exists, diffraction patterns will record the average of these. Such a pressure gradient broadens peaks and may cause the Rietveld refinement to overestimate crystallite size and/or microstrain, which also contribute to peak broadening.

Unrolled experimental diffraction patterns presented in Fig. 3 qualitatively show the degree of elastic strain due to differential stress (sinusoidal variations in peak position) and texture (variations in peak intensity). IPFs in Fig. 4 quantitatively show texture patterns. Image numbers in Table 1 correspond to numbers in the upper right-hand corner of the plots in Fig. 3 and numbers above IPFs in Fig. 4.

#### Run 1

Crystallite size of quartz slightly decreased as pressure was applied, consistent with grains being broken or divided into smaller domains, but became a little larger again during heating due to grain growth (Table 1). Stishovite nucleated during laser heating with a crystallite size of ~100 nm at 13 GPa, which decreased to ~20 nm upon compression to 23 GPa.

Initial pressure in the sample chamber was 2 GPa, and differential stress on quartz was −4.28 GPa (Table 1). Differential stress ( $t$ ), signified by the waviness of peaks in Fig. 3a, became more negative with pressure (compare #9 to #37), indicating increasing compression. However, immediately after heating,  $t$  became less negative (#40, Fig. 3a). Stishovite nucleated at 13 GPa with no differential stress, but at 23 GPa,

stress had already reached  $t = -8.31$  GPa (#48, Table 1; Fig. 3a).

Texture results are displayed with IPFs showing the sample compression direction relative to crystallographic orientations in the polycrystal (Fig. 4). Orientation densities are given in m.r.d. A very weak texture maximum (1.32 m.r.d.) near (10 $\bar{1}$ 1) developed in the quartz upon compression to 13 GPa (#37, Fig. 4a). During laser heating, the quartz texture became stronger (1.85 m.r.d.), and another maximum appeared at (0001) (#40, 41, Fig. 4a). Stishovite nucleated with (001) poles preferentially aligned parallel to the compression direction with maximum m.r.d. = 2.09. Evidence of CPO is seen in the stishovite 220 peak (Fig. 3a), which has higher intensity near  $\eta = 0^\circ$ ,  $180^\circ$ , and  $360^\circ$ , and also in the 002 peak, which has higher intensity near  $\eta = 90^\circ$  and  $270^\circ$  (i.e., the compression direction). This is quantitatively shown in IPF #40,41, Fig. 4a. Upon further compression to 23 GPa, the CPO of stishovite increased to 2.42 m.r.d. (#48, Fig. 4a).

Note that the stishovite 220 peak is barely visible, and the 002 peak is not visible in #48, Fig. 3a, implying that textural information at 23 GPa derives mainly from the 110 peak, which somewhat overlaps the diffuse peak from Kapton. In addition, weaker peaks from the boron epoxy insert are seen, especially between  $2\theta \approx 8^\circ$ – $10^\circ$ . Thus, we repeated the experiment and tilted the DAC in order to reduce diffraction from the gasket material.

The sample was compressed beyond 23–56 GPa in Run 1. Pole densities for diffraction patterns above 23 GPa were irregular, perhaps due to partial transition to the CaCl<sub>2</sub> post-stishovite phase under high differential stress (Asahara et al. 2013). Stishovite and the CaCl<sub>2</sub>-type phase are very similar in structure and have nearly perfectly overlapping

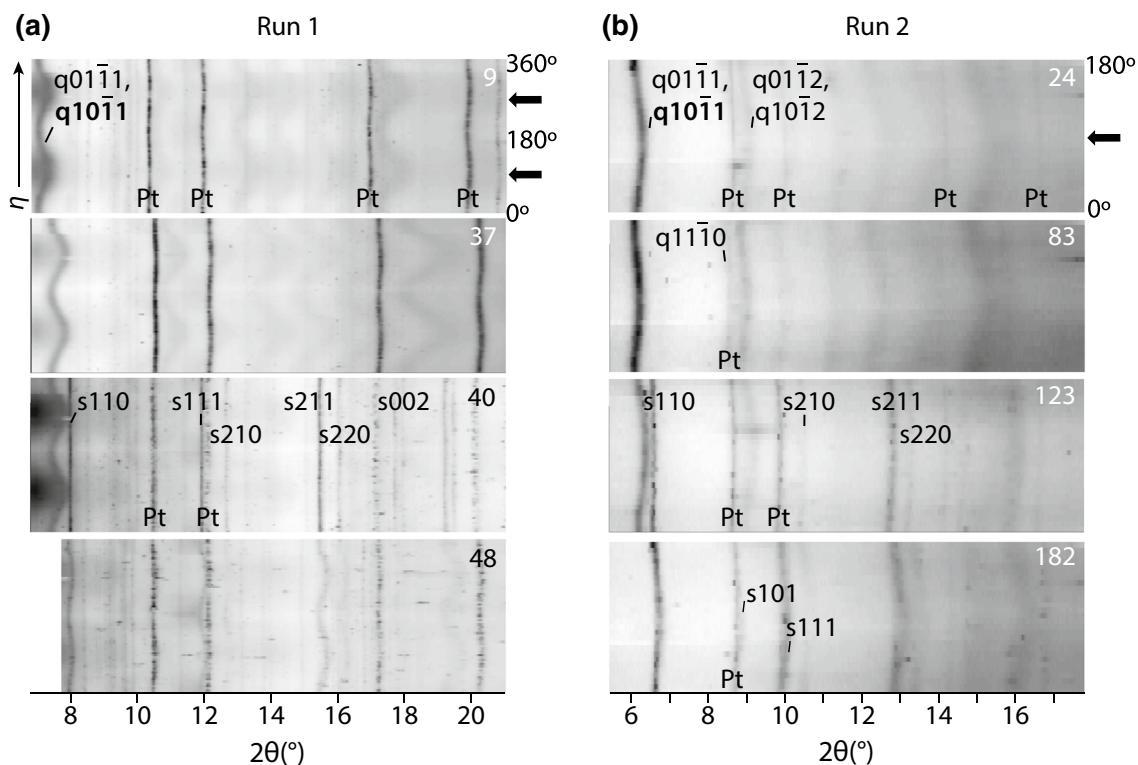


**Fig. 3** Unrolled diffraction patterns showing  $2\theta$  as a function of azimuthal angle  $\eta$  for **a** Run 1 and **b** Run 2. Numbers in the upper right corner of each pattern correspond to image numbers listed in Table 1. The compression direction is marked with arrows. Some quartz (q) and stishovite (s) peaks are labeled. Diffraction from two sets of crys-

tallographic planes in quartz contribute to overlapping peaks near  $2\theta = 6.5^\circ$ ; the  $10\bar{1}1$  peak has much higher intensity and is labeled in bold. Overlapping quartz and stishovite peaks have been left unlabeled unless one or two peaks are nearly solely responsible for the observed intensity

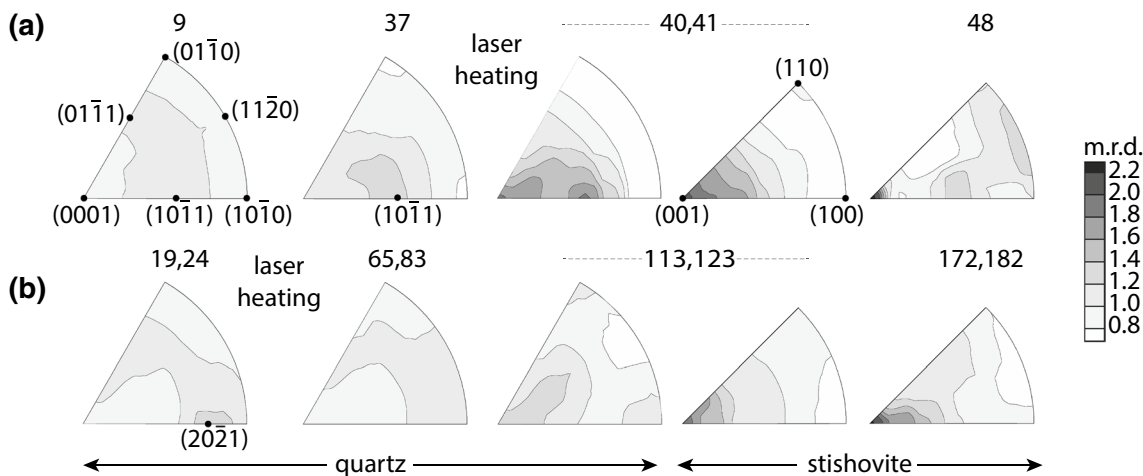


**Fig. 4** Inverse pole figures (IPFs) for **a** Run 1 and **b** Run 2 showing pole densities of crystallographic faces expressed in multiples of random distribution (m.r.d.). A sample with completely random orientation has m.r.d. = 1. Larger  $60^\circ$  slices are used to represent CPO in trigonal  $\alpha$ -quartz due to its lower symmetry, and  $45^\circ$  slices repre-

sent CPO in tetragonal stishovite. Major crystallographic directions are labeled for quartz and stishovite in (a). Cell parameters, crystallite size, differential stress ( $t$ ), and minimum and maximum pole densities corresponding to each IPF here are given in Table 1. Equal area projections

diffraction peaks that may be differentiated by comparing peak intensities. However, at high stress, diffraction peaks become diffuse, making post-stishovite peak intensities indistinguishable from stishovite peak intensities. Thus, we omitted results for the highest pressures.

## Run 2

The starting pressure in the second experiment was 16 GPa, already well into the stability field of stishovite, so the sample was heated before further compression. During laser heating, quartz crystallites grew (Table 1). Subsequent compression to 21 GPa slightly decreased quartz crystallite size and caused stishovite to nucleate with an average grain size of ~31 nm. Upon further compression, both quartz and stishovite crystallite size decreased, and at 38 GPa, quartz fully converted to stishovite, as seen by the disappearance of the quartz 01 $\bar{1}$ 1, 10 $\bar{1}$ 1, 01 $\bar{1}$ 2, and 10 $\bar{1}$ 2 peaks in #182, Fig. 3b.

Laser heating at 16 GPa caused a reduction in stress in quartz from  $t = -5.37$  to  $-4.83$  GPa. Stress increased to only  $-4.89$  GPa with subsequent compression to 21 GPa. Stishovite nucleated at 21 GPa with  $t = -4.89$  GPa as well. Compressive differential stress in stishovite increased to  $-14.0$  GPa at the highest pressure, 38 GPa, in Run 2 (Table 1).

At the beginning of Run 2, quartz had a very slight texture maximum of 1.23 m.r.d. near (20 $\bar{2}$ 1), which disappeared during heating (Fig. 4b). Another very weak maximum of 1.36 m.r.d. developed at (0001) when pressure increased to 21 GPa (#113, 123, Fig. 4b). Stishovite first appeared at 21 GPa with alignment of (001) poles parallel to the compression direction (1.93 m.r.d. maximum). At 38 GPa, the sample fully converted to stishovite, and stishovite CPO increased to 2.28 m.r.d.

## Discussion

The sample was under significant stress in both experiments, as indicated by the sinusoidal variations in peak positions (Fig. 3). Yet stishovite nucleated stress-free ( $t = 0$  GPa) in Run 1 during laser heating, as shown by straight lines (#40, Fig. 3a). However, in Run 2, stishovite did not nucleate during laser heating, which was done for a much shorter amount of time, but instead first appeared after subsequent compression to 21 GPa. Coincidentally  $t = -4.89$  GPa for both quartz and stishovite; however, the elastic strain in stishovite is much lower than in quartz, as seen in Fig. 3b, #123, where stishovite has straighter peak lines than quartz, because stishovite is elastically stiffer.

Despite differential stress during initial compression in quartz in Run 1 reaching  $-6.56$  GPa, and in Run 2,  $-5.37$  GPa, quartz develops little to no texture. A moderate

pole density (m.r.d.  $<2$ ) is observed near (10 $\bar{1}$ 1) in IPFs, especially in Run 1 (Fig. 4). Such a pattern is consistent with mechanical Dauphine twinning (Tullis 1970). The small average crystallite size of our flint and low temperature may explain the suppressed activation of substantial mechanical twinning (Tullis and Tullis 1972).

Immediately after laser heating in Run 1, the (10 $\bar{1}$ 1) maximum in quartz increased to 1.85 m.r.d., and a secondary maximum appeared at (0001) (#40, 41, Fig. 4a). This is likely due to increased differential stress—expansion of the sample from heating is prohibited by the gasket, which imposes increased pressure and stress on the sample, inducing further plastic deformation. Whereas twinning put {10 $\bar{1}$ 1} poles parallel to compression, stress-induced basal slip causes quartz crystals to preferentially reorient with their (0001) poles parallel to compression (Green 1980; Gleason et al. 1993). Similarly in Run 2, the maximum near (10 $\bar{1}$ 1) disappears during heating as crystals begin to reorient, and a (0001) maximum appears after pressure is further increased.

In both Run 1 and Run 2, stishovite nucleated with (001) poles preferentially oriented parallel to compression (Fig. 4). This texturing is unrelated to quartz texture, since the quartz-stishovite phase transition is reconstructive. Nucleation of the stishovite under stress may be responsible for its CPO; however, for nucleation in a stress field, thermodynamics predicts alignment of elastically soft directions with the principal stress (e.g., Kamb 1959; Green 1980; Shimizu 1992), while we observe the alignment of the elastically stiffest direction, [001] (Ross et al. 1990; Jiang et al. 2009), with the compression direction. It is also possible that lattice strain in the aggregate (as demonstrated by the waviness of quartz peaks in #40, Fig. 3a and #123, Fig. 3b) may have led to slip in stishovite causing newly nucleated crystals to immediately preferentially reorient. The increase in the (001) pole density maximum with further compression is attributed to slip. A recent study demonstrating capabilities of three-dimensional X-ray diffraction also observed (001) texture in 81 stishovite grains deformed at ambient temperature to 15 and 26 GPa in a DAC (Nisr et al. 2014).

We applied the Los Alamos viscoplastic self-consistent (VPSC) approach (Lebensohn and Tomé 1994) to find which slip systems are likely responsible for the (001) maximum in stishovite. VPSC simulations model deformation of grain inclusions in a homogenous, but anisotropic medium (Eshelby 1957). Deformation and rotation of lattice planes inside grain inclusions depend on the displacement gradient tensor, crystallographic orientations of grains relative to the maximum stress direction, the stress exponent  $n$  (i.e., the strain rate sensitivity to stress), crystal symmetry, and slip systems and their relative critical resolved shear stress (CRSS). The displacement gradient tensor was defined as compressive with  $\varepsilon_{11} = \varepsilon_{22} = 0.5$  and  $\varepsilon_{33} = -1$  to be consistent with experiments. Because observed



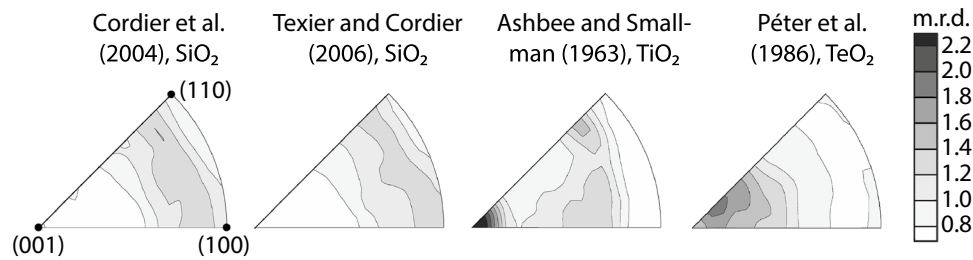


**Fig. 5** Inverse pole figures (IPFs) depicting texture development during compression to 15 % strain from four different VPSC models with slip systems and relative CRSS suggested by Cordier et al. (2004) and Texier and Cordier (2006) for stishovite ( $\text{SiO}_2$ ), Ashbee

and Smallman (1963) for rutile ( $\text{TiO}_2$ ), and Péter et al. (1986) for paratellurite ( $\text{TeO}_2$ ). Slip system activities for each model are shown in Table 2. Pole densities are measured in multiples of random distribution (m.r.d.). Equal area projections

**Table 2** Relative critical resolved shear stresses (CRSS) assigned to each slip system in VPSC simulations and the resulting percent of activity for slip systems in uniaxial compression to 15 % strain

Publication	Slip system	{100} [001]	{010} <100>	(001) <100>	{101} <10 $\bar{1}$ >	(001) <110>	{110} [001]	{021} <100>	{1 $\bar{1}$ 0} <110>	{210} <001>
Cordier et al. (2004)	CRSS	1	–	–	3	–	1	2	3	–
	Act. (%)	0.222	–	–	0.164	–	0.223	0.276	0.114	–
Texier and Cordier (2006)	CRSS	1	2	2	–	4	–	2	4	1
	Act. (%)	0.302	0.138	0.038	–	0.011	–	0.207	0.122	0.181
Ashbee and Smallman (1963)	CRSS	–	–	–	1	–	2	–	–	–
	Act. (%)	–	–	–	0.811	–	0.187	–	–	–
Péter et al. (1986)	CRSS	–	4	1	–	–	–	–	5	–
	Act. (%)	–	0.134	0.752	–	–	–	–	0.103	–

Slip systems having activities <0.01 % are not shown. Relative CRSS derive from previous microstructural studies by Cordier et al. (2004) and Texier and Cordier (2006) for stishovite ( $\text{SiO}_2$ ), Ashbee and Smallman (1963) for rutile ( $\text{TiO}_2$ ), and Péter et al. (1986) for paratellurite ( $\text{TeO}_2$ )

texture for quartz was nearly random, an initially random orientation distribution for 2,000 grains was assumed. We defined the stress exponent as  $n = 3$ , which is typical for minerals deforming in a creep regime (e.g., Barber 1990). Lastly, we chose relative CRSS based on previous microstructural studies of deformed stishovite (Cordier and Sharp 1998; Cordier et al. 2004; Texier and Cordier 2006), isostructural rutile ( $\text{TiO}_2$ ) (Ashbee and Smallman 1963; Blanchin and Fontaine 1975; Blanchin et al. 1980), and nearly isostructural paratellurite ( $\text{TeO}_2$ ) (Péter et al. 1986). IPFs derived from VPSC simulations (Fig. 5) for the different models show texture at 15 % axial shortening, calculated in increments of 1 % strain. Assumed CRSS values are shown in Table 2 and are discussed next.

We first ran VPSC simulations using relative CRSS estimated from TEM studies of deformed stishovite. Cordier and Sharp (1998), Cordier et al. (2004), and Texier and Cordier (2006) synthesized stishovite from 99.99 %  $\text{SiO}_2$  and deformed it at 14–15 GPa and 1,200–1,300 °C in a multianvil apparatus. They then examined dislocations using TEM and found [001] to be the preferred slip direction. Table 2 shows relative CRSS suggested by Cordier

et al. (2004) in their Model 1 for low pressure, which they estimated using the anisotropic elastic theory of Stroh (1958); we also ran their Model 1 for high pressure and obtained a nearly identical IPF (not shown). The resulting IPF for low pressure in Fig. 5 shows that the compression axis preferentially forms a girdle at high angles to the  $c$ -axis. Similarly, relative CRSS suggested by Texier and Cordier (2006) based on elastic energy calculations for edge dislocations (Table 2) produce a similar texture (Fig. 5). Textures obtained with VPSC simulations using relative CRSS of slip systems suggested by Cordier et al. and Texier and Cordier are both inconsistent with our results (Fig. 4).

In contrast, slip systems suggested for isostructural rutile and quasi-isostructural paratellurite produce a closer match with our experiments. Ashbee and Smallman (1963) deformed synthesized rutile ( $\text{TiO}_2$ ) single crystals in a hard-beam compression machine at  $3.4 \times 10^{-4} \text{ s}^{-1}$  strain rate, 600–1,300 °C, and ambient pressure to 3 % axial shortening and found {101}<10 $\bar{1}$ > slip to dominate and {110}[001] slip to be active to a much lesser extent. Blanchin and Fontaine (1975) and Blanchin et al. (1980) obtained

similar results for rutile at ambient pressure and temperatures between 800 and 1,700 K. Ashbee and Smallman's CRSS (Table 2) measured at <1 GPa and 750–850 °C produced a maximum pole density at (001) with a secondary maximum near (110) in VPSC simulations (Fig. 5), closely resembling our experimental results (Fig. 4). If secondary slip system {110}[001] is given a higher relative CRSS of 4, making it less active, the secondary maximum near (110) disappears, producing a texture pattern nearly identical to experimental texture at 38 GPa (#172,182, Fig. 4b). Péter et al. (1986) calculated the energy of dislocations in paratellurite (TeO<sub>2</sub>), a slightly distorted rutile structure (space group P4<sub>1</sub>2<sub>1</sub>2) using linear elastic theory of dislocations in anisotropic materials (Hirth and Lothe 1982) and predicted (001)<100>, {010}<100>, and {1 $\bar{1}$ 0}<110> to be the most likely slip systems. They then compressed single crystals below the melting temperature of 733 °C at ambient pressure in an Instron machine up to ~10 % strain at strain rates from  $3 \times 10^{-5} \text{ s}^{-1}$  to  $4 \times 10^{-5} \text{ s}^{-1}$ . Examination of dislocations with optical microscopy and X-ray topography found slip on (001)<100> to be twice as active as {010}<100> and four times more active than {1 $\bar{1}$ 0}<110>. Relative CRSS for easy slip systems in paratellurite (TeO<sub>2</sub>) based on Péter et al.'s (1986) CRSS measured at 600 °C is summarized in Table 2 along with slip activities during VPSC simulations. These slip systems also produced a maximum pole density near (001) (Fig. 5).

VPSC results suggest that pyramidal and basal slip produce the best texture match with the DAC experiments. This may be because our experiments were done at room temperature, and basal and/or pyramidal slip may dominate in stishovite at low temperatures. Prismatic slip observed in deformed stishovite by Cordier and Sharp (1998), Cordier et al. (2004), and Texier and Cordier (2006) may be typical of high temperatures.

## Conclusion

Diamond anvil cell experiments were performed in radial geometry, and diffraction patterns were collected in situ to observe CPO in stishovite during axial compression. In these room temperature experiments, we observed preferential alignment of stishovite (001) poles with the compression direction. According to polycrystal plasticity calculations, this is likely due to basal and pyramidal slip and not prismatic slip, as suggested by high temperature studies of dislocations in stishovite. These contrasting results indicate that a variety of slip systems may be active in stishovite and are dependent on conditions. As a result, stishovite's contribution to the seismic signature in the mantle may vary as a function of pressure and temperature and thus depth. This should be investigated systematically in the future with

high temperature—high-pressure deformation experiments on polycrystalline stishovite aggregates.

**Acknowledgments** This project was supported by grants from CDAC and NSF EAR 1343908. Portions of this work were performed at GeoSoilEnviroCARS (Sector 13) and at HPCAT (Sector 16), Advanced Photon Source (APS), Argonne National Laboratory. GeoSoilEnviroCARS is supported by the National Science Foundation—Earth Sciences (EAR-1128799) and Department of Energy—Geosciences (DE-FG02-94ER14466). HPCAT operations are supported by DOE-NNSA under Award No. DE-NA0001974 and DOE-BES under Award No. DE-FG02-99ER45775, with partial instrumentation funding by NSF. APS is supported by DOE-BES, under Contract No. DE-AC02-06CH11357. P. Kaercher is grateful to Jung-Fu Lin for the use of his diamond anvil cells and to Alastair MacDowell for discussion and advice. Suggestions from reviewers improved the manuscript and are much appreciated.

## References

- Andraut D, Fiquet G, Guyot F, Hanfland M (1998) Pressure-induced landau-type transition in stishovite. *Science* 282:720–724
- Angel RJ, Allan DR, Miletich R, Finger LW (1997) The use of quartz as an internal pressure standard in high-pressure crystallography. *J Appl Crystallogr* 30:461–466
- Asahara Y, Hirose K, Ohishi Y, Hirao N, Ozawa H, Murakami M (2013) Acoustic velocity measurements for stishovite across the post-stishovite phase transition under deviatoric stress: implications for the seismic features of subducting slabs in the mid-mantle. *Am Mineral* 98:2053–2062
- Ashbee KHG, Smallman RE (1963) The plastic deformation of titanium dioxide single crystals. *Proc Royal Soc A* 274:195–205
- Barber DJ (1990) Regimes of plastic deformation—processes and microstructures: an overview. In: Barber DJ, Meredith PG (eds) *Deformation Processes in Minerals, Ceramics and Rocks*. The Mineralogical Society Series 1, Unwin Hyman, London, pp 138–178
- Blanchin MG, Fontaine G (1975) Transmission electron microscope observations of deformed rutile (TiO<sub>2</sub>). *Physica Status Solidi A* 29:491–501
- Blanchin MG, Fontaine G, Kubin LP (1980) Dynamic strain aging in stoichiometric rutile single crystals. *Philos Mag A* 41:261–280
- Carpenter MA, Hemley RJ, Mao HK (2000) High-pressure elasticity of stishovite and the P4(2)/mnm phase transition. *J Geophys Res: Solid Earth* 105:10807–10816
- Chao ECT, Littler J (1963) Additional evidence for the impact origin of the Ries basin, Bavaria. *Geol Soc Am Abstr, Germany* 127
- Chao ECT, Fahey JJ, Littler J, Milton DJ (1962) Stishovite, SiO<sub>2</sub>, a very high pressure new mineral from Meteor Crater, Arizona. *J Geophys Res* 67:419–421 UC
- Cohen RE (1991) Bonding and elasticity of stishovite SiO<sub>2</sub> at high pressure: linearized augmented plane wave calculations. *Am Mineral* 76:733–742
- Cordier P, Sharp TG (1998) Characterization of dislocations in stishovite by large angle convergent beam electron diffraction. *Phys Chem Miner* 25:548–555
- Cordier P, Mainprice D, Mosenfelder JL (2004) Mechanical instability near the stishovite-CaCl<sub>2</sub> phase transition: implications for crystal preferred orientations and seismic properties. *Eur J Mineral* 16:387–399
- EI Goresy A, Dubrovinsky L, Sharp TG, Chen M (2004) Stishovite and post-stishovite polymorphs of silica in the Shergotty meteorite: their nature, petrographic settings versus theoretical

- predictions and relevance to Earth's mantle. *J Phys Chem Solids* 65:1597–1608
- Eshelby JD (1957) The determination of the elastic field of an ellipsoidal inclusion, and related problems. *Proc Royal Soc Lond* 241:376–396
- Gleason GC, Tullis J, Heidelbach F (1993) The role of dynamic recrystallization in the development of lattice preferred orientations in experimentally deformed quartz aggregates. *J Struct Geol* 15(9/10):1145–1168
- Green HW (1980) On the thermodynamics of non-hydrostatically stressed solids. *Philos Mag A* 41(5):637–647
- Haines J, Léger JM, Gorelli F, Hanfland M (2001) Crystalline post-quartz phase in silica at high pressure. *Phys Rev Lett* 87:155503
- Hammersley AP, Svensson SO, Hanfland M, Fitch AN, Häusermann D (1996) Two-dimensional detector software: from real detector to idealised image or two-theta scan. *High Press Res* 14:235–248
- Hemley RJ, Mao HK, Gramsch SA (2000) Pressure-induced transformations in deep mantle and core minerals. *Mineral Mag* 64(2):157–184
- Hirth J, Lothe J (1982) *Theory of dislocations*. Wiley, New York
- Irifune R, Ringwood AE (1993) Phase transformations in subducted oceanic crust and buoyancy relationships at depths of 600–800 km in the mantle. *Earth Planet Sci Lett* 117:101–110
- Jiang F, Gwanmesia G, Dyuzheva T, Duffy T (2009) Elasticity of stishovite and acoustic mode softening under high pressure by Brillouin scattering. *Phys Earth Planet Inter* 172:235–240
- Joswig W, Stachel T, Harris JW, Baur WH, Brey GP (1999) New Ca-silicate inclusions in diamonds—tracers from the lower mantle. *Earth Planet Sci Lett* 173:1–6
- Kamb WB (1959) Theory of preferred crystal orientation developed by crystallization under stress. *J Geol* 67(2):153–170
- Karki BB, Warren MC, Stixrude L, Ackland GJ, Crain J (1997) Ab initio studies of high-pressure structural transformations in silica. *Phys Rev B: Condens Matter* 55:3465–3471
- Kimizuka H, Ogata S, Li J, Shibusaki Y (2007) Complete set of elastic constants of  $\alpha$ -quartz at high pressure: a first-principles study. *Phys Rev B* 75:054109
- Kingma K, Cohen R, Hemley R, Mao HK (1995) Transformation of stishovite to a denser phase at lower-mantle pressures. *Nature* 374:243–245
- Kingma KJ, Mao HK, Hemley RJ (1996) Synchrotron X-ray diffraction of  $\text{SiO}_2$  to multimegabar pressures. *High Press Res* 14:363–374
- Lebensohn R, Tomé C (1994) A self-consistent viscoplastic model: prediction of rolling textures of anisotropic polycrystals. *Mater Sci Eng A* 175:71–82
- Lee CY, Gonze X (1997)  $\text{SiO}_2$  stishovite under high pressure: dielectric and dynamical properties and the ferroelastic phase transition. *Phys Rev B Condens Matter* 56:7321–7330
- Liermann HP, Merkel S, Miyagi L, Wenk HR, Shen G, Cynn H, Evans WJ (2009) Experimental method for in situ determination of material textures at simultaneous high pressure and high temperature by means of radial diffraction in the diamond anvil cell. *Rev Sci Instrum* 80:104501
- Lin JF, Mao Z, Yavaş H, Zhao J, Dubrovinsky L (2010) Shear wave anisotropy of textured hcp-Fe in the Earth's inner core. *Earth Planet Sci Lett* 298:361–366
- Liu L, Zhang J, Green HW II, Jin Z, Bozhilov KN (2007) Evidence of former stishovite in metamorphosed sediments, implying subduction to >350 km. *Earth Planet Sci Lett* 263:180–191
- Lutterotti L, Scardi P (1990) Simultaneous structure and size-strain refinement by the Rietveld method. *J Appl Crystallogr* 23:246–252
- Lutterotti L, Matthies S, Wenk HR, Schultz AS, Richardson JW Jr (1997) Combined texture and structure analysis of deformed limestone from time-of-flight neutron diffraction spectra. *J Appl Phys* 81(2):594–600
- Martini JEJ (1978) Coesite and stishovite in the Vredefort Dome, South Africa. *Nature* 272:715–717
- Martini JEJ (1991) The nature, distribution and genesis of coesite and stishovite associated with pseudotachylite of the Vredefort Dome, South Africa. *Earth Planet Sci Lett* 103:285–300
- Matthies S, Vinel GW (1982) On the reproduction of the orientation distribution function of textured samples from reduced pole figures using the concept of conditional ghost correction. *Physica Status Solidi B* 112:K111–K114
- Matthies S, Priesmeyer HG, Daymond MR (2001) On the diffractive determination of single-crystal elastic constants using polycrystalline samples. *J Appl Crystallogr* 34:585–601
- Merkel S, Yagi T (2005) X-ray transparent gasket for diamond anvil cell high pressure experiments. *Rev Sci Instrum* 76:046109
- Nisr C, Ribárik G, Ungár T, Vaughan GBM, Merkel S (2014) Three-dimensional X-ray diffraction in the diamond anvil cell: application to stishovite. *High Press Res: An Int J* 34(2):158–166
- Péter A, Fries E, Janszky J, Castaing J (1986) Dislocations in paratellurite  $\text{TeO}_2$ : elastic energies and plastic deformation. *Rev de Phys Appl* 21(5):289–298
- Prakapenka VP, Shen G, Dubrovinsky LS, Rivers ML, Sutton SR (2004) High pressure induced phase transformation of  $\text{SiO}_2$  and  $\text{GeO}_2$ : difference and similarity. *J Phys Chem Solids* 65:1537–1545
- Prakapenka VP, Kubo A, Kuznetsov A, Laskin A, Shkurikhin O, Dera P, Rivers ML, Sutton SR (2008) Advanced flat top laser heating system for high pressure research at GSECARS: application to the melting behavior of germanium. *High Press Res* 28(3):225–235
- Rietveld HM (1969) A profile refinement method for nuclear and magnetic structures. *J Appl Crystallogr* 2:65–71
- Ross N, Shu J-F, Hazen RM (1990) High-pressure crystal chemistry of stishovite. *Am Mineral* 75:739–747
- Shen G, Wang L, Ferry R, Mao HK, Hemley RJ (2010) A portable laser heating microscope for high pressure research. *J Phys: Conf Ser* 215:012191
- Shimizu I (1992) Nonhydrostatic and nonequilibrium thermodynamics of deformable materials. *J Geophys Res* 97(4):4587–4597
- Shoemaker EM, Chao ECT (1961) New evidence for the impact origin of the Ries Basin, Bavaria, Germany. *J Geophys Res* 66:3371–3378
- Sinclair W, Ringwood AE (1978) Single crystal analysis of the structure of stishovite. *Nature* 272:714–715
- Singh AK, Balasingh C, Mao HK, Hemley RJ, Shu J (1998) Analysis of lattice strains measured under nonhydrostatic pressure. *J Appl Phys* 83(12):7567–7575
- Stishov SM, Belov NV (1962) Crystal structure of a new dense modification of silica  $\text{SiO}_2$ . *Proc USSR Acad Sci* 143(4):951
- Stishov SM, Popova SV (1961) New dense polymorphic modification of silica. *Geochemistry* 10:923–926
- Stroh AN (1958) Dislocations and cracks in anisotropic elasticity. *Phil Mag* 3:625–646
- Teter DM, Hemley RJ, Kresse G, Hafner J (1998) High pressure polymorphism in silica. *Phys Rev Lett* 80(10):2145–2148
- Texier M, Cordier P (2006) TEM characterization of dislocations and slip systems in stishovite deformed at 14 GPa, 1,300 C in the multianvil apparatus. *Phys Chem Miner* 33:394–402
- Toby B (2006) *R* factors in Rietveld analysis: how good is good enough? *Powder Diffr* 21(1):67–70
- Tsuchida Y, Yagi T (1989) A new, post-stishovite high-pressure polymorph of silica. *Nature* 340:217–220
- Tullis J (1970) Quartz: preferred orientation in rocks produced by Dauphiné twinning. *Science* 168:1342–1344

- Tullis J, Tullis T (1972) Preferred orientation of quartz produced by mechanical Dauphiné twinning: thermodynamics and axial experiments. *Flow fract Rocks: Am Geophys Union Geophys Monogr* 16:67–82
- Vinnik L, Kato M, Kawakatsu H (2001) Search for seismic discontinuities in the lower mantle. *Geophys J Int* 147:41–56
- Wang F, Tange Y, Irifune T, Funakoshi K (2012) P-V-T equation of state of stishovite up to mid-lower mantle conditions. *J Geophys Res* 117:B06209
- Wenk HR, Matthies S, Donovan J, Chateigner D (1998) Beartex: a Windows-based program system for quantitative texture analysis. *J Appl Crystallogr* 31:262–269
- Wenk HR, Lonardelli I, Merkel S, Miyagi L, Pehl J, Speziale S, Tommaseo CE (2006) Deformation textures produced in diamond anvil experiments, analyzed in radial diffraction geometry. *J Phys: Condens Matter* 18:S933–S947
- Wenk HR, Lutterotti L, Kaercher P, Kanitpanyacharoen W, Miyagi L, Vasin R (2014) Rietveld texture analysis from synchrotron diffraction images: II. Complex multiphase materials and diamond anvil cell experiments. *Powder Diffr*. doi:[10.1017/S0885715614000360](https://doi.org/10.1017/S0885715614000360)
- Yoneda A, Cooray T, Shatskiy A (2012) Single-crystal elasticity of stishovite: new experimental data obtained using high-frequency resonant ultrasound spectroscopy and a gingham check structure model. *Phys Earth Planet Inter* 190–191:80–86